PCCP

PAPER

View Article Online
View Journal | View Issue

Cite this: *Phys. Chem. Chem. Phys.*, 2025, **27**, 21504

Steric substitution in phenylazo indoles reveals interplay of steric and electronic effects on photophysical dynamics

Christian A. Guzman, Zachary J. Knepp, Allen H. Chen, Jacob Haber, Rachel Joh, Gabriel B. Masso, Lisa A. Fredin * and Elizabeth R. Young *

Indole-containing azo dyes have the potential to add photocontrol to pharmaceuticals, as substituted indoles are prevalent in biological systems. It is critical to understand the complex interplay substitution has on the photophysical properties in order to enable control of the on and off states of a drug. This work identifies the impact of steric and electronic effects of four steric R-groups on the photoisomerization and thermal reversion processes of a series of phenylazo indole dyes and demonstrates that protonation can be used to control bulk isomerization. Four phenylazo indole dyes were synthesized with varying steric bulk, a proton (H), a methyl group (Me), a *tert*-butyl group (*t*Bu), or a phenyl group (Ph), at the C_2 position of the indole adjacent to the azo bond. 2D NOESY NMR and computational methods were used to identify the rotational conformation of each *trans*-isomer as the *anti*-rotamer. The *cis*-isomer of the unsubstituted moiety accesses the *eclipsed*-rotamer while all other dyes adopt the *anti*-rotamer after photoexcitation. The Taft and Charton free energy models were employed to identify if the steric or electronic contributions of the steric R-group more strongly impact photoisomerization and thermal reversion dynamics. Surprisingly, in these indole dyes, electron donation strength, measured by the electronic Taft parameter of the steric R-group, correlated with the increasing photoisomerization rate. Thermal reversion rates were found to decrease with increasing steric substitution following the steric Taft parameter. However, the unsubstituted compound deviated from the trends in both photoisomerization and reversion dynamics. Acidity constants increase with increasing bulk of the steric R-group using the Charton steric model and protonation of the azo bond eliminated bulk photoisomerization. Thus, the impact of steric modification does not result in straightforward effects on the photophysical behavior, even when choosing a site close to the azo bond.

Received 23rd May 2025,
Accepted 11th September 2025

DOI: 10.1039/d5cp01953b

rsc.li/pccp

Introduction

Azo dyes have garnered much attention in recent years because of their common use as textiles, cosmetics, and food colorants owing to their synthetic accessibility, ease of synthetic scalability, and high stability under ambient conditions. They are also commonly used chromophores for pH indication[1] and metal ion sensing applications.[2] These compounds are well known to undergo a photoinduced *trans* → *cis* isomerization about the N=N bond, which is observed and tracked spectroscopically.[3–13]

The photoisomerization mechanism of azobenzene and other azo dyes has been well studied. The main absorption in such dyes is generally accepted to occur through a $\pi \rightarrow \pi^*$ excitation.[9,10,14] Relaxation of the excited state has been shown to occur through a torsional rotation of the CNNC dihedral angle or inversion of the CNN bond angle.[10,15,16] Non-radiative relaxation to the ground state occurs through an $S_1 \rightarrow S_0$ conical intersection[11,17] that allows, in most azo dyes, a population of the metastable *cis*-isomer to form. The coinciding isomerization has been leveraged in applications such as optical data storage,[18–22] molecular machinery,[23] and photopharmacology.[24–27] Elucidating the role that structural modification plays in a variety of azo systems is crucial to the rational design of molecules with desired photophysical properties.

The photophysics and applications of substituted azobenzenes have been extensively studied.[28–32] A series of 3,3′,5,5′-tetrasubstituted aliphatic azobenzenes showed that increasing steric hinderance increases the thermal reversion half-life from hours to tens of hours in DMSO and *n*-octane.[33] Noncovalent interaction analysis shows that London dispersion forces between substituents stabilizes the *cis*-isomer, leading to a longer observed thermal reversion time.[33] Additionally, noncovalent interactions

Department of Chemistry, Lehigh University, Bethlehem, Pennsylvania 18015, USA. E-mail: ery317@lehigh.edu, laf218@lehigh.edu

play a role in transition state conformation of arylazo pyrazoles.[34] While there is a large body of literature on aryl azo dyes, structural modification is primarily limited to addition and placement of functional groups and ring-size expansion.

Introduction of heteroaryl groups offers a way to access diverse electronic configurations leading to unique photophysics based on heteroatom identity and position.[35] Heteroatoms allow for hydrogen bonding,[36–39] coordination to transition metal complexes,[40–43] and additional protonation sites[28] that expand the versatility of these compounds. Azopyridines have been incorporated into polymer systems as pendant groups, which allows for the formation of unique supramolecular architectures.[36,37]

Our prior work[12] on phenylazo pyridines identified the importance of the nitrogen heteroatom position relative to the azo bond on the photophysics of the moiety. The protonation state of the dye impacts photoisomerization and thermal reversion rates, even when protonation occurs on the pyridine ring rather than on the azo bond.[12] An asymmetric heterocycle with respect to the azo bond gives rise to both *anti*- and *eclipsed*-rotamers identified using a combination of experimental transient absorption and computed density functional theory (DFT) difference spectra.[44] While protonation of the heterocycle seems to completely shut down bulk photoisomerization of the azo compounds on the millisecond timescale (*i.e.* using UV-vis spectroscopy), isomerization and thermal reversion is observable on ultrafast timescales.

Indole-containing azo compounds are of particular interest due to the prevalence of substituted indoles in biological systems and pharmaceuticals. Combining the bioactive nature of indoles with the photoactivity of the azo group allows for the control of activity based on conformation. Phenylazo amido indole compounds act as *cis*-photoagonists to the $h\mathrm{CB}_1$ receptor[45] while a phenylazo $N'N'$ dimethyl tryptamine molecule acts as a *trans*-agonist to the 5-HT_{2A} receptor.[46] Both of these classes of molecules provide a useful tool to pharmacologists to tease out complex signaling mechanisms and active site conformation to design molecules for clinical applications.

Recent work systematically explored the photophysical properties of non-methylated phenylazo indoles.[47–49] Changing the solvent environment from aprotic to protic allows a hydrazone intermediate to form *via* solvent-assisted intermolecular proton transfer from the indole N–H.[47] *N*-Methylation of the indole nitrogen increases thermal reversion lifetimes by several orders of magnitude, from ms to hours, depending on solvent choice, by shutting off the hydrazone pathway.[47] Additionally, for the non-methylated indoles, increasing steric substitution by addition of a methyl group was shown to decrease the stability of the *cis*-isomer, speeding up reversion.

This work builds on these insights and applies them to phenylazo indole photophysics by examining steric and electronic contributions that arise when a steric R-group is installed adjacent to the azo bond. Herein, we report the synthesis, characterization, and photoisomerization and thermal reversion lifetimes of a series of *N*-methylated phenylazo indole dyes as a function of the steric bulk of the C_2 R-group on the indole (Fig. 1). The naming convention OMe-PAI-R is used to denote the substituents

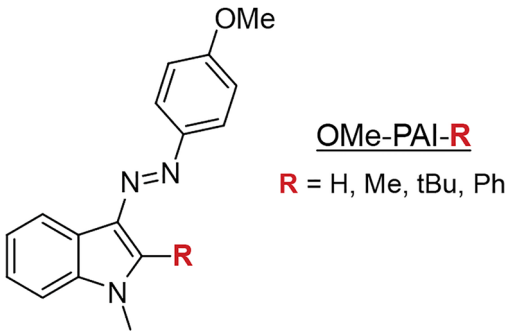

Fig. 1 General structure of sterically substituted phenylazo indoles.

attached to the PhenylAzo Indole (PAI) scaffold. For example, OMe-PAI-R denotes a methoxy group on the *para* phenyl position and R denotes a steric substituent on the indole carbon adjacent to the azo bond (C_2), which in this work is either a proton (H, unsubstituted), a methyl group (Me), a *tert*-butyl group (*t*Bu), or a phenyl group (Ph). A combination of 2D-NMR, UV-vis spectroscopy, and DFT are employed to identify the rotameric conformation of the *cis*-isomers and intrinsic photophysical properties. This work identifies multiple factors impacting photoisomerization and thermal reversion dynamics. The complex interplay of steric and electronic effects are key parameters for rational design of molecular structures for applications.

Experimental

Synthesis

Generally, one equivalent of (*p*)-anisidine was added to 1 mL of HBF_4 (50% aq.) and cooled to 0 °C in an ice bath. A cold aqueous solution of 1 eq. $NaNO_2$ was added dropwise to form a diazonium salt. The solution was stirred for approximately 10 minutes. The resulting diazonium salt solution was added dropwise to a solution containing one equivalent of a C_2 substituted 1-methyl indole in glacial acetic acid. The solution quickly turned deep red and was left to stir at room temperature. The resulting mixture was purified by aqueous workup and extraction with ethyl acetate. The solution was dried with $MgSO_4$. Solvent was removed *in vacuo* followed by crystallization in hot 90% ethanol. Detailed synthetic procedures for each compound as well as ^{1}H NMR (with proton assignment) and ^{13}C NMR spectra are presented in the SI.

Photoisomerization and thermal reversion studies

Fresh stock solutions of the azo molecules were prepared in dry acetonitrile (MeCN) at 0.3 mM. Solutions were prepared for analysis by diluting the stock solution in 5.00 mL of MeCN to a concentration of 0.1 μM. 2.0 mL of the dilute solution was transferred to a 1-cm quartz cuvette and placed in the sample holder of an OceanOptics Flame UV-vis spectrophotometer. The *trans* → *cis* isomerization was observed by monitoring the spectral change over time upon illumination with a LuzChem LEDi-HUV7 lamp head (λ_{max} = 375 nm, whm = 12 nm) and LuzChem LED Illuminator at 337 mW (0.98 A). Spectra were collected every 65 ms.

Once a photostationary state was achieved, the illumination source was removed and spectra indicating thermally induced reversion were collected. All isomerization and reversion experiments were performed in the dark with a blackout cloth covering the lamp and sample holder to limit ambient light, which impacts the kinetics of the forward and reverse processes. Isomerization and reversion lifetimes were determined by taking kinetic traces of the absorption change at the maximum wavelength of the *trans*-isomer feature and fitting the trace to a monoexponential decay model using OriginPro 2024.

2D NOESY (nuclear Overhauser effect spectroscopy) NMR rotamer analysis

Samples were prepared by dissolving the solid dye in 1 mL of deuterated N,N-dimethylformamide (DMF) to create a 10 mM solution. This solution was then passed through a 0.22-micron nylon filter into a Norell S500 7'' valved VT NMR tube, which had been washed with acetone and dried in an oven overnight. The sample was triply freeze-pump-thawed and brought to a pressure of 6–10 torr. The spectrometer temperature was lowered to −30 °C to limit thermal reversion of the *cis*-isomer over the course of the experiment. The *cis*-isomer was formed through illumination with the same equipment described in the photoisomerization section above. Details of the data acquisition including pulse sequence, number of scans, mixing time, and data processing information are described in the instrumentation section of the SI.

Acid titrations and pK_a value determination

A stock solution of each dye was prepared at a concentration of 0.9 mM in a 5.00 mL volumetric flask using dry MeCN. Dilute unprotonated solutions (A) were prepared at ∼0.2 μM (1 AU) depending on the molecule. Protonated solutions (B) were prepared at the same concentration as A with the addition of *p*-toluenesulfonic acid monohydrate (TosOH) at a concentration of 14 mM. 2.0 mL of solution A was transferred to a 1-cm quartz cuvette. Acid titrations were performed by monitoring spectral changes upon addition of small volumes (0.1–10 μL) of B using a Hamilton syringe. Increasing addition volume was necessary to provoke a consistent amount of change in the absorption spectrum.

Quantum mechanical calculations

DFT and time-dependent DFT (TD-DFT) calculations were performed using Gaussian16[50] using the CAM-B3LYP functional,[51,52] 6-311G(d,p) basis set,[53] Grimme's D3BJ dispersion correction,[54] and a polarizable continuum model of acetonitrile.[55] *Anti*- and *eclipsed–trans* and *cis* structures were confirmed to be local minima by zero imaginary frequencies. Absorption spectra were calculated using the first 20 singlet excitations. Optimized transition states were verified to have one negative frequency.

The rotational ground-state singlet (S_0) surfaces of the dyes tracking the *trans* → *cis* isomerization were determined from relaxed scans of the azo CNNC dihedral angle, in which only the dihedral angle was frozen. The first and second singlet excited-state (S_1 and S_2) energies were calculated from vertical TD-DFT excitations at each optimized geometry along the rotational ground-state curve.

Results

Rotamers of the *trans*- and *cis*-isomers: DFT predictions and conformational analysis by ^{1}H and 2D NOESY NMR

In addition to the well-known *trans*- and *cis*-isomers that are commonly discussed in azo literature, these phenylazo indole dyes can, due to the azo bond linkage at the indole C_3 position, adopt two distinct rotamers in the *trans* and *cis* configurations. The rotameric structure can be defined by the NNCC indole dihedral angle, in which the N_3 and C_2 atoms can either be *anti* or *eclipsed* with respect to the N_2–C_3 bond (highlighted in Fig. 2).

Our recently published computational work on two of these moieties predicted that OMe-PAI-H and OMe-PAI-Ph exist primarily in the *anti–trans* conformation.[56] Optimization (Fig. 3) of the *anti–trans*- and *eclipsed–trans*-isomer structures of OMe-PAI-Me and OMe-PAI-*t*Bu shows that these molecules also exist in the *anti–trans* ground state. Boltzmann populations at 300 K, derived from DFT calculated energies, predict that the *anti–trans* structure is favored over the *eclipsed–trans* and make up >96% of the ground-state population for OMe-PAI-H and >99% for the OMe-PAI-Me, -*t*Bu, and -Ph (Table S5).

To experimentally verify the rotameric structure of the *trans*-isomers, interspacial interactions were investigated using 2D NOESY NMR. The 2D NOESY NMR spectra of the *trans*-isomers (Fig. S1–S4) show only interspacial interactions between the protons on the R-groups and the protons of the neighboring indole N–CH_3 group that would be present in either rotamer, meaning that the *trans*-rotamer cannot be experimentally assigned.

The energies computed for the optimized *cis* structures indicate that the lowest-energy *cis* conformer of OMe-PAI-H and OMe-PAI-Ph is *eclipsed* while OMe-PAI-Me and OMe-PAI-*t*Bu are *anti* (Fig. 4). Given the proximity of the aromatic (*p*)-methoxy phenyl protons to either the indole ring (*anti*) or the

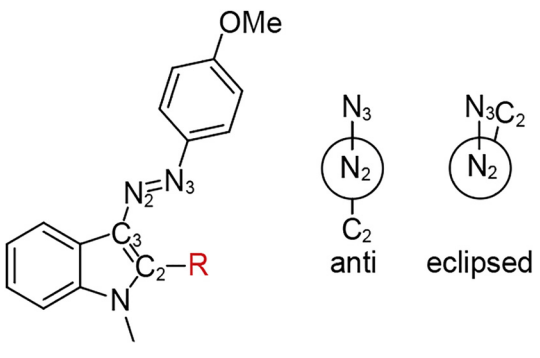

Fig. 2 *Eclipsed–trans* structure of sterically substituted phenylazo indoles with Newman projections of the *anti* and *eclipsed* rotamers based on the NNCC indole dihedral angle denoted by numbered atoms on the structure.

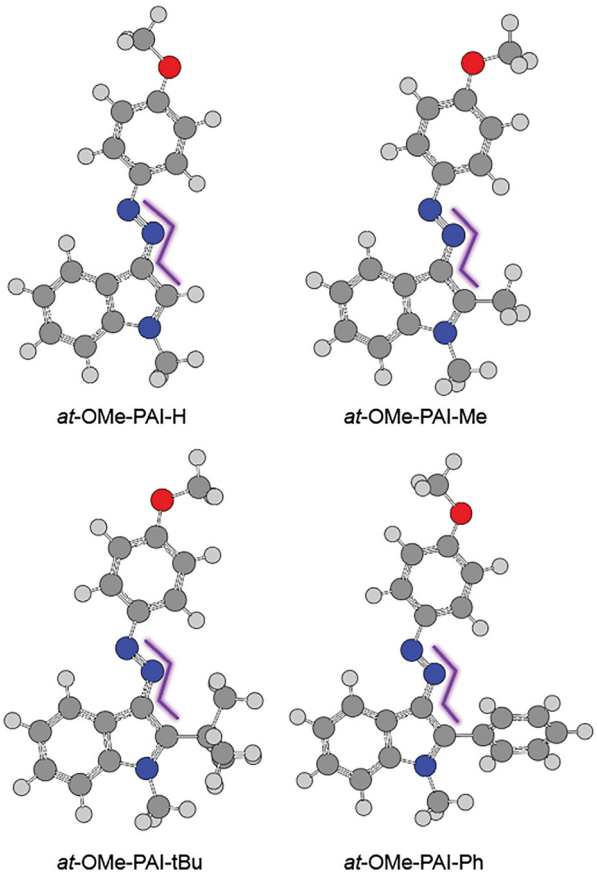

Fig. 3 Optimized *anti–trans* (abbreviated as at) structures of OMe-PAI-H (top left), OMe-PAI-Me (top right), OMe-PAI-*t*Bu (bottom left), and OMe-PAI-Ph (bottom right). The NNCC dihedral angle that defines the rotamer identity is shown by the purple line ("Z" shape – *anti*). CAM-B3LYP/6-311G(d,p)-D3BJ/PCM(MeCN).

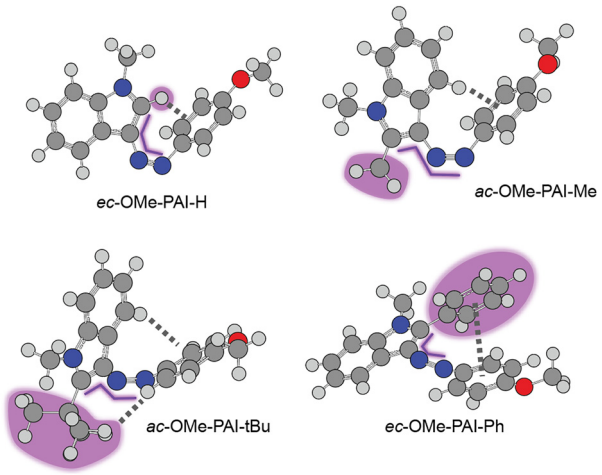

Fig. 4 Optimized *cis*-isomer structures of *eclipsed*-OMe-PAI-H, *anti*-OMe-PAI-Me, *anti*-OMe-PAI-*t*Bu, and *eclipsed*-OMe-PAI-Ph. *ec* is used to label *eclipsed–cis*-isomers, ac is used to label *anti–cis*-isomers. The R-groups are highlighted in purple to assist in orienting the observer. The NNCC dihedral angle that defines the rotamer identity is shown by the purple line ("Z" shape – *anti*; "C" shape – *eclipsed*). Relevant interspacial interactions for each rotamer are shown with grey dotted lines. CAM-B3LYP/6-311G(d,p)-D3BJ/PCM(MeCN).

R-group (*eclipsed*), interspacial interactions were expected to be strong enough to make a conformational assignment *via* 2D NOESY NMR (Fig. 4, grey dotted lines).

To experimentally determine the rotameric conformation of the *cis*-isomers, samples were photolyzed until the maximum *cis*-isomer conversion was achieved and then immediately brought to the pre-cooled NMR spectrometer. The *cis*-isomer of OMe-PAI-H was confirmed to be in an *eclipsed* conformation based on the cross peaks observed between the R-group and both doublets on the (*p*)-methoxy phenyl ring (Fig. S5, and indicated by the grey dashed line in Fig. 4).

The 2D NOESY NMR spectrum of OMe-PAI-Me reveals that, as predicted, it adopts an *anti–cis* conformation, indicated by the interaction of the proton on the phenyl portion of the indole closest to the azo bond with the doublet attributed to the (*p*)-methoxy phenyl protons closest to the azo bond (Fig. S6, grey dashed line in Fig. 4).

The rotameric structure of *cis*-OMe-PAI-*t*Bu could not be assigned using 2D NOESY NMR because both the *t*Bu group and the doublet on the phenyl portion of the indole ring are observed to interact with the doublets of the (*p*)-methoxy phenyl ring (Fig. S7, grey dashed lines in Fig. 4). Optimized structures of the *anti*- and *eclipsed–cis*-isomers show that the relevant protons in each of these structures are within the spin diffusion limited range and therefore it is no surprise that both are observable in the 2D spectrum. Observation of both sets of cross peaks makes experimental assignment of the *cis*-isomer impossible through NOESY cross peak identification. Boltzmann populations, however, indicate that OMe-PAI-*t*Bu preferentially adopts the *anti–cis* conformation by >99% (Table S5).

The 2D NOESY NMR spectrum of the OMe-PAI-Ph *cis*-isomer shows the same cross peak interactions as those observed in OMe-PAI-Me and thus is experimentally assigned as an *anti–cis*-isomer (Fig. S8). While the *eclipsed–cis*-OMe-PAI-Ph is computationally lower in energy, a higher barrier between the *anti–cis* and *eclipsed–cis* on the S_0 and S_1 surfaces seems to limit access to the *eclipsed*-rotamer experimentally.[56]

In addition to the 2D NOESY cross peaks, the protons used to identify each of the rotamers exhibit upfield shifts in the 1D ^{1}H NMR spectra of greater than 2 ppm compared to the corresponding *trans*-isomer spectra for each *cis*-isomer (Fig. S9). Upfield shifting indicates greater electronic shielding that is attributed to the closer proximity of protons on the opposite aromatic ring system that would be present in the *cis*-isomer.

Ground-state characteristics

The primary absorption feature of OMe-PAI-H, -Me, -*t*Bu, and -Ph (Fig. 5) are at 380 nm, 385 nm, 387 nm and 392 nm, respectively (Table 1). While an increase in steric hinderance is generally associated with a blue shift in absorption maxima that arises due to a loss of planarity resulting in a break in conjugation, addition of steric bulk at the C_2 position of the indole ring results in a red shift of the primary feature by 5, 7, and 12 nm for R = Me, *t*Bu, Ph, respectively (Fig. S10). DFT

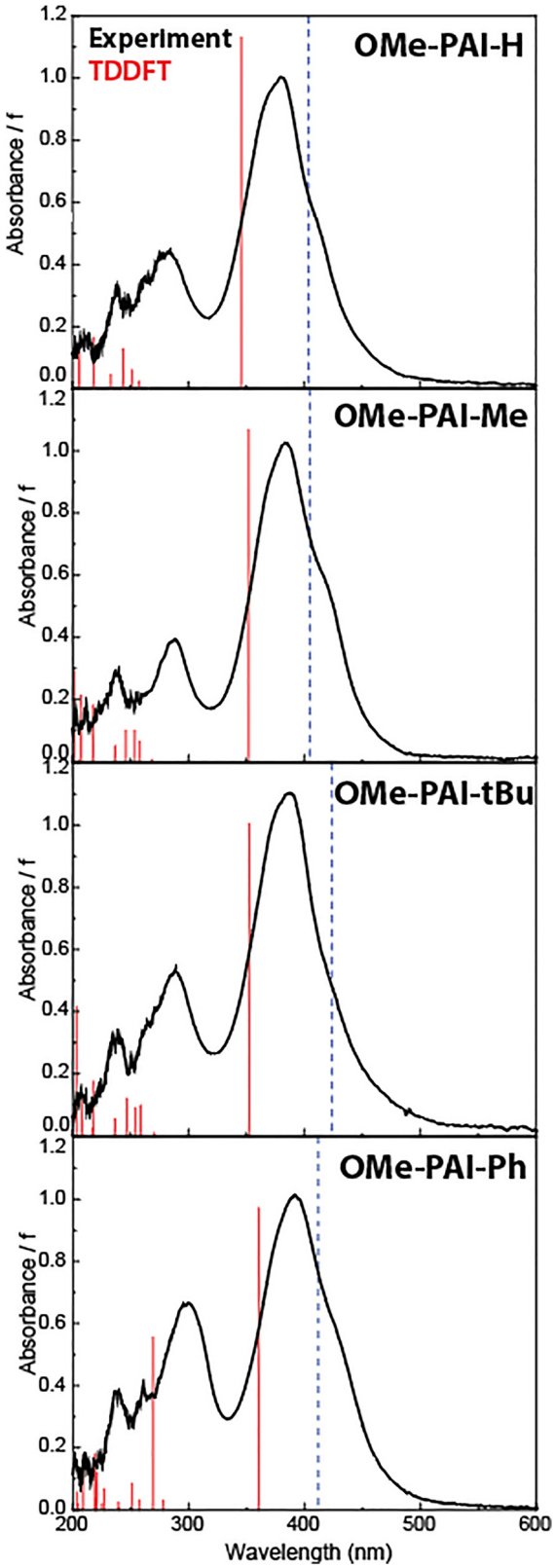

Fig. 5 The experimental absorption spectra (black) and first 20 singlet transitions (red) of OMe-PAI-H, OMe-PAI-Me, OMe-PAI-*t*Bu, and OMe-PAI-Ph overlaid with each other. The lowest-energy transitions (S_1, n → π*) are symmetry forbidden with computed oscillator strengths of zero and are shown as blue dotted lines. CAM-B3LYP/6-311G(d,p)-D3BJ/PCM(MeCN).

anti–trans-optimized structures show that the planarity of the primary ring system remains largely intact even with the most sterically bulky R group (Fig. 3 and Fig. S11) due to the reduction in strain from the five-membered indole ring near the azo bond.

The R-group has little effect on the frontier molecular orbitals of the *anti–trans*-rotamers (Fig. S12–S16). The highest occupied molecular orbital (HOMO) of each *trans*-isomer is spread across the entire π-system (Fig. S12).[56] The HOMO-1 of OMe-PAI-H, -Me, and -Ph is located on the indole π-system while the HOMO-1 of OMe-PAI-*t*Bu shows indole-π electron density and azo nonbonding character. The HOMO-2 is non-bonding in each moiety. Steric substitution causes destabilization of the non-bonding HOMO-2 increasing from OMe-PAI-H to OMe-PAI-Me to OMe-PAI-*t*Bu. The R-group on OMe-PAI-Ph has a less destabilizing effect on the HOMO-2 because it is tilted relative to the indole ring. The lowest unoccupied molecular orbital (LUMO) is a π* orbital spread across the π-system for all the dyes.

The computed TD-DFT transitions closely match the experimental absorption spectra of the *trans*- and *cis*-isomers (Fig. 5 and Tables S1–S4, Fig. S17) and provide insight into the nature of the associated transitions. As in azobenzene, the primary absorption feature is attributed to the S_2 (π → π*) transition. In these dyes, the S_2 transition is solely a HOMO → LUMO transition. The small red shift of the computed *trans*-isomer S_2 going from OMe-PAI-H to OMe-PAI-Ph is a consequence of a small decrease in the HOMO–LUMO gap caused by both destabilization of the HOMO and stabilization of the LUMO. A lower-intensity red-shifted shoulder attributed to the symmetry-forbidden S_1 (n → π*) is observed in the experimental spectra. The HOMO−2, which is the primary contributor to the S_1 transition, is nonbonding (Tables S1–S4) making this a formally unallowed transition (denoted as the blue dotted line in Fig. 5). S_1 transitions in azo dyes are often forbidden, as has been reported in the TD-DFT calculated spectra of azobenzene as well as in our prior work on naphthalene- and pyridine-based azo dyes.[57] However, in solution, molecular vibrations can lead to small changes in the symmetry that makes this transition weakly-allowed and therefore observable experimentally, as is the case here.

Photoisomerization dynamics

Each azo derivative undergoes *trans* → *cis* photoisomerization upon excitation at 375 nm. The structural change is tracked using the absorption spectrum *via* a decay of the *trans*-isomer S_2 feature and concomitant growth of a weak, red-shifted feature attributed to the *cis*-isomer S_1 (Fig. 6, top, and Fig. S18). The photoisomerization lifetimes are determined using single-wavelength fitting of the absorption change at the *trans*-isomer λ_{max} to a mono-exponential decay function (Fig. 6, top inset). The isomerization lifetimes were determined to be 115.1, 169, 143.3, and 206 ms for OMe-PAI-H, -Me, -*t*Bu, and -Ph, respectively (Table 1).

Thermal reversion dynamics

After prolonged illumination, a photostationary state is achieved in which a steady-state population of *cis*-isomer is

Table 1 Summary of spectroscopic, photophysical, and conformational data and acidity constants for OMe-PAI-R

	$\lambda_{max,trans}$ (nm)	$\lambda_{max\,H,\ trans}$ (nm)	$\lambda_{max,cis}$ (nm)	τ_{Isom} (ms)	τ_{Rev} (s)	pK_a	Rotamer assignment	
							trans[a]	*cis*[b] (DFT/experimental)
-H	380	485	414	115.1 (4.1)	716 (85)	13.19 (0.34)	*anti*	*eclipsed*/*eclipsed*
-Me	385	470	458	169 (11)	3.97 (0.49)	14.18 (0.49)	*anti*	*anti*/*anti*
-*t*Bu	387	488	471	143.3 (6.8)	21.2 (2.5)	14.89 (0.49)	*anti*	*anti*/–[c]
-Ph	392	487	471	206 (18)	182 (41)	14.48 (0.21)	*anti*	eclipsed/anti

The standard deviation for each value is shown in parentheses. [a] DFT-calculated lowest energy rotamer. [b] Rotamer assignments are bolded. [c] Signals indicative of both rotamers were found.

formed. Removal of illumination from the sample allows the bulk thermal reversion process to occur. The decay of the *cis*-isomer S_1 peak coincides with a regrowth of the *trans*-isomer S_2 peak with no other process present, as indicated by clear isosbestic points in the UV-vis spectra (Fig. 6, middle, and Fig. S19).

Thermal reversion lifetimes were determined using single-wavelength fitting of the growth of the *trans*-isomer S_2 feature fit to a monoexponential decay equation (Fig. 6, middle inset). The reversion lifetimes were determined to be 716, 3.97, 21.2, and 182 s for OMe-PAI-H, -Me, -*t*Bu, and -Ph, respectively (Table 1).

Substituent impact on acidity and photophysics

Protonation of the molecules leads to a red shift in the main absorption feature by 105, 85, 101, and 95 nm for OMe-PAI-H, -Me, -*t*Bu, and -Ph, respectively (Fig. 6, bottom, and Fig. S20–S23). The pK_a values are 13.19, 14.18, 14.89, and 14.48 for OMe-PAI-H, -Me, -*t*Bu, and -Ph, respectively (Table 1) based on acid titrations with TosOH and subsequent fitting analysis.

Acid titration data was originally analyzed using the Benesi–Hildebrand equation, which resulted in a poor fit to the data. The Benesi–Hildebrand equation assumes that the ligand is present in much higher quantities than the substrate,[58] which is not the case for this system. When this occurs, the double reciprocal plots can produce non-linear trends that cannot be properly fit. Therefore, a quadratic treatment of the 1 : 1 binding isotherm was employed (see SI for more details) to determine the K_a of each dye.

The acidity constant (p$K_{a,Azo}$) of each dye was determined using the following expression,

$$pK_{a,Azo} = \log(K_a) + pK_{a,TosOH} \quad (1)$$

where K_a is the observed binding constant of the azo compound, and p$K_{a,TosOH}$ is the acidity constant of TosOH, which is taken from the literature as 8.5 in acetonitrile.[59]

Discussion

Determining steric and electronic contributions: the Taft and Charton equations

The Hammett, Taft, and Charton models are commonly used in structure–function studies.[60–64] The Hammett model describes electronic effects of *para* substituents, while the Taft and Charton models account for steric effects and can be applied to *ortho* substituents. The substitution site on these phenylazo indole moieties occurs on the indole ring adjacent to the central point of geometric change in the molecule, which operates as a pseudo-*ortho* site, necessitating an expanded model that accounts for steric effects. The Taft and Charton models, described below, are used to determine steric effects in asymmetric catalysis[64] and to relate structure to biological activity.[65,66]

The Taft free energy relation[67] (eqn (2)) is derived from the kinetic rates of the acid and base catalyzed hydrolysis of methyl esters. Since the substituent site is directly next to the reaction site for these compounds, both steric and electronic parameters were included in the following relation,

$$\log\frac{k_R}{k_{Me}} = \rho^*\sigma^* + \delta E_s \quad (2)$$

where k_R is the rate constant of a process with the substituent of interest, k_{Me} is the rate constant of the same process with a methyl substituent, ρ^* is the electronic sensitivity factor, σ^* is the electronic substituent constant describing inductive and field effects, δ is the steric sensitivity factor, and E_S is the steric substituent constant (Table 2).

Analyzing the rate (or lifetime) of a process as a function of the R-group can be accomplished independently using either the $\sigma^\star$ or E_S parameter. The parameter that produces the best linear trend indicates whether that the process is more strongly impacted by field and inductive ($\sigma^\star$) or steric (E_S) effects.

The Charton steric model, originally described as the modified Taft equation,[70] seeks to describe rate trends purely in terms of steric effects using the relation,

$$\log k_R = \Psi\nu + h \quad (3)$$

where k_R is the rate of the process with a substituent of interest, ν is the difference between the van der Waals radius of a group and the H atom (Table 2), Ψ is the steric sensitivity factor, and h is a regression factor that holds no physical meaning.[64,71,72]

Rather than using observed kinetic rate constants to determine steric and electronic parameters, as was done in the Taft formalism, Charton used van der Waals radii of functional groups and correlated those values to rate constants. This model assumes that groups are spherical, which may make it unsuitable for linear correlations to be made when large substituents are studied.

Deviations from linearity in each of these models may indicate a change in mechanism if there are multiple linear

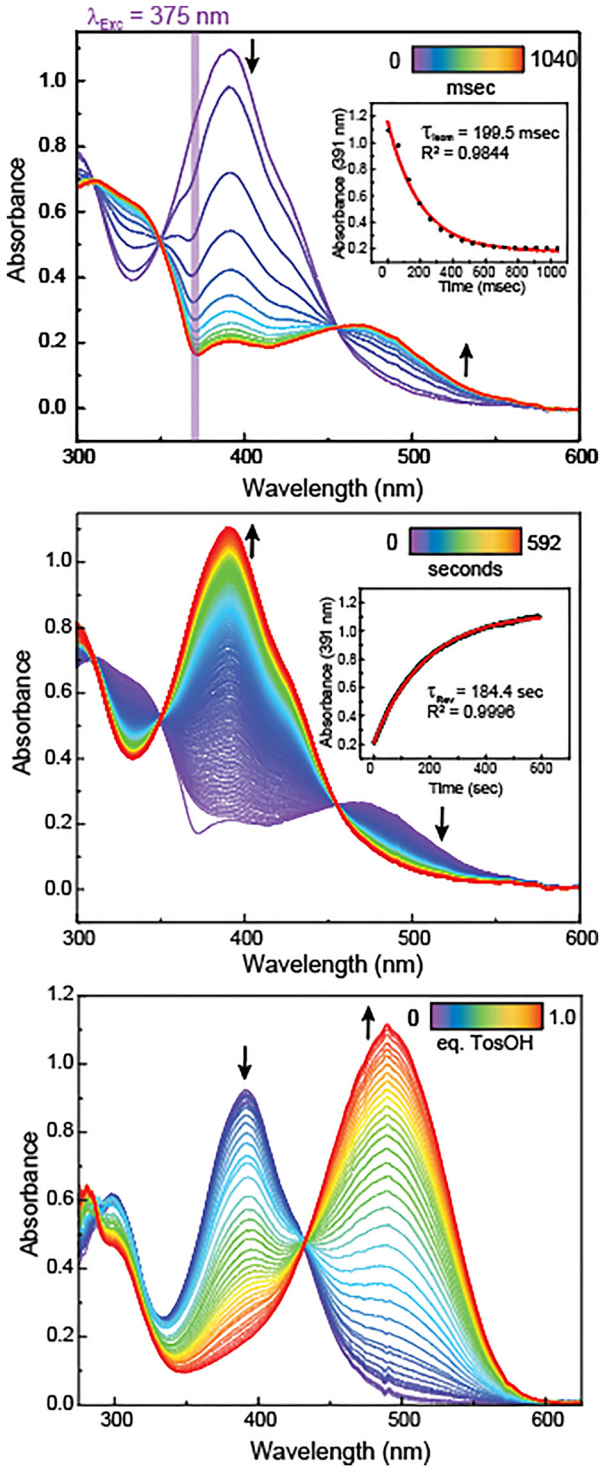

Fig. 6 (top) UV-vis spectra indicating *trans* → *cis* photoisomerization of OMe-PAI-Ph. The inlayed graph shows the kinetic trace at λ_{max} and the resulting lifetime. (Middle) UV-vis spectra indicating *cis* → *trans* thermal reversion of OMe-PAI-Ph and (bottom) photometric acid titration of OMe-PAI-Ph showing a red shift in absorbance after sequential acid additions.

regimes.[60,68] Single point deviations can also occur when modification of the structure enables the molecular scaffold to adopt a different conformation or undergo a process inaccessible to other molecules in the series.[61–63,69] Such deviations

Table 2 Electronic and steric Taft parameters (σ^* and E_S, respectively) and Charton steric parameter, ν

-R	σ^*	E_S	ν
-H	0.49	1.24	0.00
-Me	0.00	0.00	0.52
-*t*Bu	-0.30	-1.54	1.24
-Ph	0.60	-2.55	0.57

are a result of the simplicity inherent to the model. A deviation in photoisomerization and thermal reversion would reasonably be expected for OMe-PAI-H in these studies on the basis that it adopts the *eclipsed–cis* rotamer while all others adopt the *anti–cis* rotamer upon photoisomerization. The primary pathway for *both* photoisomerization and thermal reversion processes would therefore be different, which is not accounted for in the Taft model. Such non-linearity can provide qualitative insight into the system outside of rate prediction.

The Taft and Charton models were applied to photoisomerization, thermal reversion, and acidity constant data to identify whether steric or electronic effects more strongly impact these processes in this series of sterically substituted phenylazo indoles. The models determined to best capture these trends are shown in Fig. 7. A side-by-side comparison of each model is shown in Fig. S25.

Electronic effects would be expected to be the primary influence on photoisomerization lifetimes through modification of the excited-state potential energy surface curvature and minima. Steric size is expected to influence the height of the ground-state barriers resulting in a larger buildup of *cis*-isomer population (due to slower reversion kinetics, *vide infra*). Steric groups may also influence the excited-state pathway (*i.e.* rotation or inversion) as was shown to occur in *ortho*-substituted azobenzenes.[73,74]

Photoisomerization

Plotting the photoisomerization lifetime as a function of the steric Taft parameter, E_S, shows a linear trend in lifetimes for only OMe-PAI-H, -Me, and -Ph (Fig. S25D). The Charton model indicates that there may be a mechanistic shift because the plot of isomerization lifetime as a function of the Charton parameter shows a modest V shape (Fig. S25J). However, the rotational potential energy curves (PECs) show no unexpected curvature (Fig. S26) that would indicate different mechanisms in the photoisomerization of the complexes. These observations indicate that sterics likely do not have the largest effect on the photoisomerization.

A plot of the photoisomerization lifetime as a function of the electronic Taft parameter, σ^*, shows an apparent linear relationship between OMe-PAI-Me, -*t*Bu, and -Ph (Fig. 7, top). It is possible that an exponential relationship would be observed by using substituents that are larger than R = Ph. Indeed, we attempted the synthesis of a mesityl-substituted OMe-PAI but encountered synthetic limitations of the starting material. Stronger electron donating character of the R-group leads to shorter isomerization lifetimes (*i.e.* faster photoisomerization rates)

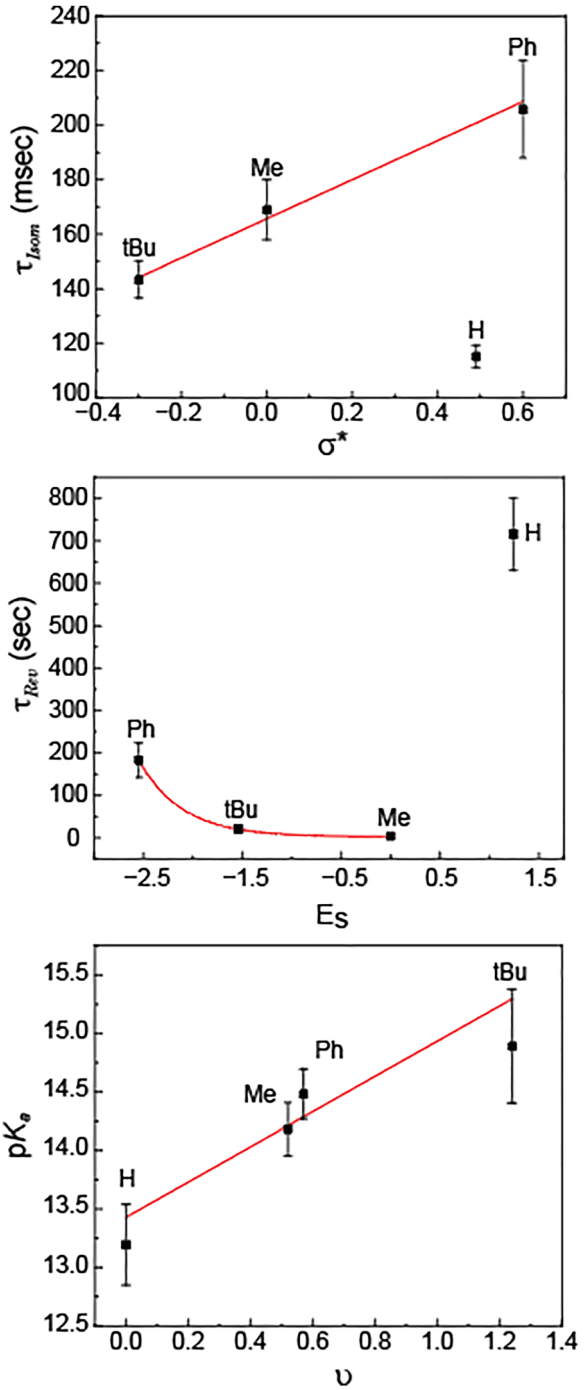

Fig. 7 (Top) Photoisomerization lifetimes plotted against the electronic Taft parameter, σ^*. (Middle) Thermal reversion lifetimes plotted against the Taft steric parameter, E_S. (Bottom) Trend in pK_a values based on Charton's steric parameter, ν.

except in the case of OMe-PAI-H. Our prior computational study analyzing the full S_1 rotational/inversional surfaces of OMe-PAI-H and OMe-PAI-Ph rationalized this observation as arising from an energy plateau in OMe-PAI-Ph S_1 region between the indole CNN angles of ~135–165° that is not captured in the 2D surfaces presented in the SI.[56] The presence of plateau slows the isomerization process in OMe-PAI-Ph compared to OMe-PAI-H. On the other hand, the OMe-PAI-H S_1 shows a steady decline in energy in that region that results in fast conversion.[56] Given the linear trend in photoisomerization lifetime between OMe-PAI-Ph, -Me, and -*t*Bu, OMe-PAI-Me and OMe-PAI-*t*Bu likely contain similar S_1 plateaus. These plateaus would increase the lifetime of the excited state and increase the observed photoisomerization lifetime relative to OMe-PAI-H, causing OMe-PAI-H to lie off of the trendline created by the other three moieties. This phenomenon has been reported for the excited states of other systems.[75,76]

Thermal reversion

Based on previous reports on *ortho*-phenylazo pyrazoles[77] and phenylazo indoles,[47] it was expected that the thermal reversion lifetime of these compounds would decrease upon substitution from R = H to R = Me and that the more sterically hindered compounds (R = Me, *t*Bu, Ph) would follow the steric Taft model. However, the trend was not so straightforward for these phenylazo indoles.

Plotting the thermal reversion lifetime as a function of the steric Taft parameter, E_S, shows an expected exponential relationship for OMe-PAI-Me, -*t*Bu, and -Ph (Fig. 7, middle) in which increasing hinderance increased the thermal reversion lifetime (*i.e.* slowed the reversion rate). In the Taft plot using the steric parameter, OMe-PAI-H breaks the exponential trend, indicating that a factor besides sterics influences the thermal reversion process for this molecule.

A similar trend in thermal reversion lifetime emerges in the electronic Taft plot (Fig. S25B). A summated steric and electronic Taft plot ($E_S + \sigma^*$) has extremely similar curvature to the steric Taft plot, which indicates that thermal reversion is primarily dominated by steric factors with little contribution from electronic modulation (Fig. S25H). The trend between reversion lifetime and steric substitution aligns with general physical chemistry intuition that increasing hinderance increases rotational energy barriers.

Charton's model (Fig. S25K) results in a near-linear relationship between thermal reversion lifetime and steric bulk, with OMe-PAI-Me as an outlier. However, our experimental and computational structures show OMe-PAI-Me should be similar to OMe-PAI-*t*Bu, which is also aliphatic. Thus, there is no evidence that the Charton model should be used over the Taft model to describe thermal reversion properties.

OMe-PAI-H thermal reversion considerations

The unsubstituted dye, OMe-PAI-H, might be expected to have the shortest thermal reversion lifetime because it is physically the smallest group. However, experimentally OMe-PAI-H reverts on the slowest timescale. Interestingly, OMe-PAI-H is the only moiety to adopt an *eclipsed–cis* conformation, as the other compounds form an *anti–cis* conformation upon photoillumination (*vide supra*). The *eclipsed–cis* orientation in OMe-PAI-H is stabilized through an η^6–H interaction (Fig. 4) that is disrupted upon substitution. Instead, the other moieties adopt *anti–cis* conformations that are stabilized through indole–H interactions with the phenyl ring. This indicates a more complex reversion path from *eclipsed–cis* to *anti–trans* for OMe-PAI-H.

Additionally, transition state calculations indicate that variations to the steric R-group substituent impact the mechanism of *cis* → *trans* thermal reversion (Fig. S29, S30 and Table S6). For these moieties, several different types of transition states are optimizable. For OMe-PAI-H, one phenyl inversion and one indole-inversion transition state from the *eclipsed–cis* and from the *anti–cis* were found. For OMe-PAI-Me, two indole inversional transition states from the *eclipsed–cis* and three rotational transition states from the *anti–cis* were found. For OMe-PAI-*t*Bu, two indole inversion transition states from the *eclipsed–cis*, two rotations from the *anti–cis*, and one phenyl inversion from the *anti–cis* were found. For OMe-PAI-Ph, one indole inversion and one phenyl inversion from the *eclipsed–cis*, two phenyl inversions from *anti–cis*, and one rotational transition state from the *anti–cis* were found. Inversional transition states are defined as those containing a linear N═N–C bond. A T-shaped geometry is obtained for every inversional transition state in each of the moieties, indicating that the reversion mechanism through these states is a rotationally-assisted inversion in all cases, and never purely inversional. Pure rotational transition states, however, are optimized in these systems that exhibit CNNC dihedral angles of ∼100°.

Photoisomerization and thermal reversion pathways

Thermal reversion lifetimes are dictated by the activation energy between the photogenerated *cis*-rotamer and lowest energy transition states along the pathway back to the lowest-energy *trans*-isomer. In general, for these phenlyazo indoles, substitution decreases the energy needed to access the transition state and decreases the expected *cis*-isomer lifetime (*i.e.* increases the reversion rate) (Table S6). The process of *cis* → *trans* reversion differs for OMe-PAI-H compared to OMe-PAI-Me, -*t*Bu and -Ph. Reversion of OMe-PAI-H involves moving from a primarily *eclipsed–cis* to a primarily *anti–trans* isomer. Calculations reveal that the transition states connecting the *eclipsed–cis* to *eclipsed–trans* and *anti–cis* to *anti–trans* are a rotationally-assisted indole inversion (Fig. 8, blue lines). The *anti-* and *eclipsed*-rotamers of each isomer are connected by low-barrier pathways that lead to fast interconversion between the rotamer states. Therefore, the rate of thermal reversion is dominated by the *cis* → *trans* process and the transition state accessed upon those transitions. In contrast, the reversion of OMe-PAI-Me, -*t*Bu, and -Ph involve moving from a primarily *anti–cis* to an *anti–trans* isomer. Calculations reveal that the transition states connecting the *anti–trans* and *anti–cis* isomers of OMe-PAI-Me and OMe-PAI-*t*Bu are primarily lower-barrier rotational transition states, with some contribution from an indole inversion from *eclipsed–cis* to *eclipsed–trans.* The transition state connecting the *anti–trans* and *anti–cis* isomers of OMe-PAI-Ph is a mixed rotational/phenyl-inversional pathway (Fig. 8, black lines). Despite the *anti–cis*-isomer being the dominant conformation of OMe-PAI-Me and OMe-PAI-*t*Bu, the *eclipsed*-rotamer could act as a low-energy funnel for these moieties that would increase the thermal reversion rate because the *eclipsed–cis* → *eclipsed–trans* barrier is relatively low in energy (Fig. 8, grey funnel). Specifically, for OMe-PAI-Me, there is an

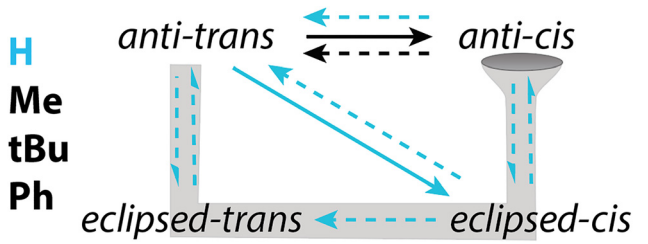

Fig. 8 Photoisomerization (solid) and thermal reversion (dotted) pathways of OMe-PAI-H (blue) and OMe-PAI-Me/-*t*Bu/-Ph (black). For all compounds, there is a fast equilibrium between *anti-* and *eclipsed*-rotamers in the *cis*- and *trans*-isomers. The grey funnel represents the low energy barrier pathway through the *eclipsed–cis* to *eclipsed–trans* for OMe-PAI-Me, -*t*Bu, and -Ph.

eclipsed–cis to *eclipsed–trans* inversional path that is approximately 0.15 eV lower than the lowest *anti–cis* → *anti–trans* rotational barrier. Therefore, we expect that the experimental thermal reversion lifetimes are a weighted summation of the *eclipsed–cis* → *eclipsed–trans* and *anti–cis* → *anti–trans* processes (Table S6). The result is that rotation pathways in these phenylazo indole dyes consist of lower-barrier transitions that lead to faster reversion of OMe-PAI-Me, -*t*Bu, and -Ph compared to OMe-PAI-H.

Rotational transition states of azo compounds are commonly difficult to determine using DFT because of the conical intersection between the S_0 maximum and S_1 minimum that can cause convergence failure. Additionally, rotation around the azo bond necessitates that the azo π-bond breaks and reforms.[16,78] Bond breakage typically causes the rotational thermal reversion pathway to be significantly higher in energy than the inversional pathway. Thus, it is unusual that the phenylazo indoles have one or more optimized rotational transition states and that they are either near or lower in energy than the inversional transition states. Interestingly, no rotational transition states were found for OMe-PAI-H. The rotational PEC of OMe-PAI-H has a broader conical intersection region (Fig. S26) and multiple guess geometries from the scan curve never resulted in an optimized transition state. Further, removing R-groups from the rotational transition states of other dyes also failed to result in an optimized transition state.

Generally, the thermal reversion lifetimes are determined by the photochemically formed *cis*-rotamer and accessibility from that rotamer to low-energy transition states back to the lowest energy *trans*-isomer. OMe-PAI-H reverts through rotationally-assisted inversional pathways that are higher in energy than the lowest barriers of the substituted OMe-PAI-Me, -*t*Bu, and -Ph moieties. Access to the *eclipsed–cis*-rotamer of OMe-PAI-Me, -*t*Bu, and -Ph due to low-barriers between rotamers might enable fast thermal reversion *via* a low-energy *anti–cis* → *eclipsed–cis* → *eclipsed–trans* → *anti–trans* thermal pathway. The influence of the thermal reversion mechanism on the lifetime is primarily steric in nature. Despite the large population of *anti–cis* formed upon excitation of the sterically hindered dyes, the *eclipsed–cis* → *eclipsed–trans* pathways cannot be discounted from an energetic perspective.

Substituent impact on acidity and photophysics

The acidity of a molecule can be significantly influenced by steric bulk if the protonation site is close to the R-group. This, however, does not necessarily rule out the electronic effect of substituents. DFT shows that protonation of all the dyes occurs on the phenylazo N, which indicates steric effects from the R-groups on the indole should be attenuated (Fig. S31). The TD-DFT for the lowest energy protonated structures closely matches experimental spectra (Fig. S32). Addition of electron donating groups *ortho* to the azo bond should increase the electron density on the azo nitrogens and decrease their acidity.

Plotting the pK_a value with either the steric or electronic Taft parameters shows a linear trend for OMe-PAI-H, -Me, and -*t*Bu (Fig. S25C and F). An increase in electron donation (σ^*) and steric bulk (E_S) result in a decrease in acidity. OMe-PAI-Ph deviates from this trend, possibly because the Taft parameters are derived from the hydrolysis of aliphatic esters and assumes a constant resonance effect. The deviation of OMe-PAI-Ph is present in the combined Taft plot ($\sigma^* + E_S$) as well.

A plot using Charton's steric model[71] shows a convincing linear relationship between pK_a value and steric bulk (Fig. 7, bottom). While the phenyl ring is not in the plane of the main structure, it still contributes electron density to the delocalized system and stabilizes the charge induced by protonation. The linear nature of the relation between steric bulk and acidity indicates that acidity change in this series of molecules is primarily steric in nature.

Protonation of the molecules impedes the bulk photoisomerization process, making it undetectable by UV-vis spectroscopy (Fig. S33). In a similar manner to phenylazo naphthalenes[79] and pyridines, protonation of the azo bond increases the rate for thermal reversion by decreasing the S_0 rotational potential energy barrier thereby limiting a significant buildup of the *cis*-isomer population and enabling ultrafast thermal reversion. Additionally, the rotational S_1 minimum is shifted towards the *trans*-isomer geometry, preferring to relax into a vibrationally excited *trans*-like geometry rather than accessing the *cis*-geometry (Fig. S34).

Conclusion

In summary, we present a series of *N*-methylated phenylazo indoles bearing R-groups of varying size on the indole ring adjacent to the azo bond. Photophysical properties were examined using a combination of spectroscopic and computational methods. Trends between photophysics and structure were assessed using the Taft and Charton free energy relations. The results indicate that predicting photophysical behavior in azo dyes should go beyond a purely steric lens.

Through 2D NOESY NMR, the Me, *t*Bu and Ph substituted dyes were identified to adopt an *anti–cis* conformation while the unsubstituted dye adopts an *eclipsed–cis* conformation. Photoisomerization lifetimes were found to decrease with increasing donor character of the substituent, according to the Taft electronic model. Thermal reversion lifetimes of the substituted dyes were shown to increase exponentially with increased hinderance, according to the Taft steric model. DFT-calculated ground state barriers indicate that the unsubstituted dye undergoes a rotationally-assisted inversional pathway while the substituted dyes undergo primarily rotational reversion pathways. The *cis*-isomer lifetime of the unsubstituted dye is elongated due to the higher barrier of the inversional thermal reversion pathway. The substituted dyes possess low energy reversion pathways from the higher energy *eclipsed–cis* → *eclipsed–trans* pathway. The influence that such rotamers have on photophysical properties should be considered when studying asymmetric photoswitches.

Protonation was observed to induce a red shift in the absorption spectrum and limit bulk photoisomerization. The reversible nature of this process offers a binary way to control the photophysics through changes to the solvent environment of the molecule. This work provides insight into the rational design of heterocyclic azo compounds for applications that require extended *cis*-isomer lifetimes.

Author contributions

CAG – experimental investigation, synthesis and characterization, formal analysis, writing (original draft); ZJK, AHC – computational investigation, formal analysis; JH, RJ – experimental data validation; GM – computational data validation; LAF – conceptualization, supervision, writing (review/editing); ERY – conceptualization, supervision, writing (original draft/review/editing).

Conflicts of interest

There are no conflicts to declare.

Data availability

Data for figures is available at **https://github.com/the-young-lab/2025-indole-azo-sterics.git**.

Supplementary information: Detailed synthetic information of each compound as well as ^{1}H NMR (with proton assignment), ^{13}C NMR, 2D NOESY NMR, photoisomerization spectra, thermal reversion spectra, photometric acid titrations, binding constant Python program, and unprotonated/protonated PECs. See DOI: **https://doi.org/10.1039/d5cp01953b**.

Acknowledgements

1D and 2D NMR experiments made use of the Lehigh University (LU) NMR Facility. The Bruker Avance NEO spectrometer was acquired through NSF-MRI-1725883, with additional support from LU. Acknowledgment is made to the Donors of the American Chemical Society Petroleum Research Fund for support of this research (PRF #65343-ND6). ERY and LAF thank The Pittsburgh Foundation for funding (UN2020-114823). Portions of this research were conducted with research computing resources provided by LU and the TG-CHE190011

allocation from XSEDE, which is supported by NSF grant number ACI-1548562. Financial support also comes from LU.

References

1 H. Wenker, Indicator Properties of Dinitroaniline Azo Dyestuffs, *Ind. Eng. Chem. Anal. Ed.*, 1935, **7**(1), 40–41, DOI: 10.1021/ac50093a020.
2 Y.-W. Shi, X.-Q. Liu, P. Shi and X.-Y. Zhang, Characterization of Zinc-Binding Properties of a Novel Imidase from Pseudomonas Putida YZ-26, *Arch. Biochem. Biophys.*, 2010, **494**(1), 1–6, DOI: 10.1016/j.abb.2009.11.016.
3 G. S. Hartley, The *cis*-Form of Azobenzene, *Nat. Chem.*, 1937, **140**, 281.
4 T. Fujino and T. Tahara, Femtosecond Time-Resolved Fluorescence Study of Photoisomerization of Trans -Azobenzene, *J. Phys. Chem. A*, 2001, **2**, 8123–8129.
5 T. Fujino and T. Tahara, Picosecond Time-Resolved Raman Study of trans-Azobenzene, *J. Phys. Chem. A*, 2000, 4203–4210.
6 I. K. Lednev, T. Ye, R. E. Hester and J. N. Moore, Femtosecond Time-Resolved UV-Visible Absorption Spectroscopy of trans-Azobenzene in Solution, *Chem. Phys. Lett.*, 1996, **3654**(96), 13338–13341.
7 T. Schultz, J. Quenneville, B. Levine, A. Toniolo, T. J. Martínez, S. Lochbrunner, M. Schmitt, J. P. Shaffer, M. Z. Zgierski and A. Stolow, Mechanism and Dynamics of Azobenzene Photoisomerization, *J. Am. Chem. Soc.*, 2003, **125**(27), 8098–8099, DOI: 10.1021/ja021363x.
8 M. Quick, A. L. Dobryakov, M. Gerecke, C. Richter, F. Berndt, I. N. Ioffe, A. A. Granovsky, R. Mahrwald, N. P. Ernsting and S. A. Kovalenko, Photoisomerization Dynamics and Pathways of trans- and *cis*-Azobenzene in Solution from Broadband Femtosecond Spectroscopies and Calculations, *J. Phys. Chem. B*, 2014, **118**(29), 8756–8771, DOI: 10.1021/jp504999f.
9 C. Chang, Y. Lu, T. Wang and E. W. Diau, Photoisomerization Dynamics of Azobenzene in Solution with S_1 Excitation: A Femtosecond Fluorescence Anisotropy Study, *J. Am. Chem. Soc.*, 2004, **29**, 10109–10118.
10 H. M. D. Bandara and S. C. Burdette, Photoisomerization in Different Classes of Azobenzene, *Chem. Soc. Rev.*, 2012, **41**(5), 1809–1825, DOI: 10.1039/c1cs15179g.
11 I. Conti, M. Garavelli and G. Orlandi, The Different Photoisomerization Efficiency of Azobenzene in the Lowest nπ* and ππ* Singlets: The Role of a Phantom State, *J. Am. Chem. Soc.*, 2008, **16**, 5216–5230.
12 S. M. Martin, Z. J. Knepp, I. A. Thongchai, K. Englehart, K. Sorto, A. Jaffer, L. A. Fredin and E. R. Young, The Doorstop Proton: Acid-Controlled Photoisomerization in Pyridine-Based Azo Dyes, *New J. Chem.*, 2023, **47**, 11882–11889, DOI: 10.1039/D3NJ01769A.
13 S. W. Magennis, F. S. Mackay, A. C. Jones, K. M. Tait, P. J. Sadler, V. Recei, V. No, V. Re, M. Recei and V. February, Two-Photon-Induced Photoisomerization of an Azo Dye, *Chem. Mater.*, 2005, **7**, 2059–2062.
14 Y. Hirose, H. Yui and T. Sawada, Effect of Potential Energy Gap between the n-π* and the π–π* State on Ultrafast Photoisomerization Dynamics of an Azobenzene Derivative, *J. Phys. Chem. A*, 2002, **106**(13), 3067–3071, DOI: 10.1021/jp0138375.
15 E. M. M. Tan, S. Amirjalayer, S. Smolarek, A. Vdovin, F. Zerbetto and W. J. Buma, Fast Photodynamics of Azobenzene Probed by Scanning Excited-State Potential Energy Surfaces Using Slow Spectroscopy, *Nat. Commun.*, 2015, **6**(1), 5860, DOI: 10.1038/ncomms6860.
16 P. Tavadze, G. Avendaño Franco, P. Ren, X. Wen, Y. Li and J. P. Lewis, A Machine-Driven Hunt for Global Reaction Coordinates of Azobenzene Photoisomerization, *J. Am. Chem. Soc.*, 2018, **140**(1), 285–290, DOI: 10.1021/jacs.7b10030.
17 E. Wei-Guang Diau, A New Trans-to-Cis Photoisomerization Mechanism of Azobenzene on the S_1 (n, π*) Surface, *J. Phys. Chem. A*, 2004, **108**(6), 950–956, DOI: 10.1021/jp031149a.
18 A. I. Kovalchuk, Y. L. Kobzar, I. M. Tkachenko, Y. I. Kurioz, O. G. Tereshchenko, O. V. Shekera, V. G. Nazarenko and V. V. Shevchenko, Photoactive Fluorinated Poly(Azomethine)s with Azo Groups in the Main Chain for Optical Storage Applications and Controlling Liquid Crystal Orientation, *ACS Appl. Polym. Mater.*, 2020, **2**(2), 455–463, DOI: 10.1021/acsapm.9b00906.
19 S. Manickasundaram, P. Kannan, Q. M. A. Hassan and P. K. Palanisamy, Azo Dye Based Poly(Alkyloxymethacrylate)s and Their Spacer Effect on Optical Data Storage, *J. Mater. Sci.: Mater. Electron.*, 2008, **19**(11), 1045–1053, DOI: 10.1007/s10854-007-9450-y.
20 M. C. Spiridon, K. Iliopoulos, F. A. Jerca, V. V. Jerca, D. M. Vuluga, D. S. Vasilescu, D. Gindre and B. Sahraoui, Novel Pendant Azobenzene/Polymer Systems for Second Harmonic Generation and Optical Data Storage, *Dyes Pigments*, 2015, **114**(C), 24–32, DOI: 10.1016/j.dyepig.2014.10.010.
21 E. Madiahlagan, S. B N, Z. Ngaini and G. Hegde, Synthesis, Liquid Crystalline Properties and Photo Switching Properties of Coumarin-Azo Bearing Aliphatic Chains: Application in Optical Storage Devices, *J. Mol. Liq.*, 2019, **292**, 111328, DOI: 10.1016/j.molliq.2019.111328.
22 J. Wang, B. Wu, S. Li, G. Sinawang, X. Wang and Y. He, Synthesis and Characterization of Photoprocessable Lignin-Based Azo Polymer, *ACS Sustainable Chem. Eng.*, 2016, **4**(7), 4036–4042, DOI: 10.1021/acssuschemeng.6b00975.
23 O. S. Bushuyev, M. Aizawa, A. Shishido and C. J. Barrett, Shape-Shifting Azo Dye Polymers: Towards Sunlight-Driven Molecular Devices, *Macromol. Rapid Commun.*, 2018, **39**(1), 1–14, DOI: 10.1002/marc.201700253.
24 M. Wegener, M. J. Hansen, A. J. M. Driessen, W. Szymanski and B. L. Feringa, Photocontrol of Antibacterial Activity: Shifting from UV to Red Light Activation, *J. Am. Chem. Soc.*, 2017, **139**(49), 17979–17986, DOI: 10.1021/jacs.7b09281.
25 A. M. Schulte, D. Kolarski, V. Sundaram, A. Srivastava, F. Tama, B. L. Feringa and W. Szymanski, Light-Control over Casein Kinase 1δ Activity with Photopharmacology: A Clear Case for Arylazopyrazole-Based Inhibitors, *Int. J. Mol. Sci.*, 2022, **23**(10), 5326, DOI: 10.3390/ijms23105326.

26 M. J. Fuchter, On the Promise of Photopharmacology Using Photoswitches: A Medicinal Chemist's Perspective, *J. Med. Chem.*, 2020, **63**(20), 11436–11447, DOI: 10.1021/acs.jmedchem.0c00629.

27 L. Wang, M. Chen, S. Xia, Z. Xu, Y. Li and X. Shao, Azobenzene-Diamides as Photopharmacological Ligands for Insect Ryanodine Receptor, *J. Agric. Food Chem.*, 2020, **68**(49), 14409–14416, DOI: 10.1021/acs.jafc.0c03272.

28 S. Mehrparvar, Z. N. Scheller, C. Wölper and G. Haberhauer, Design of Azobenzene beyond Simple On-Off Behavior, *J. Am. Chem. Soc.*, 2021, **143**(47), 19856–19864, DOI: 10.1021/jacs.1c09090.

29 N. K. Joshi, M. Fuyuki and A. Wada, Polarity Controlled Reaction Path and Kinetics of Thermal *cis*-to- Trans Isomerization of 4-Aminoazobenzene, *J. Phys. Chem. B*, 2014, **118**(7), 1891–1899.

30 C. J. Otolski, A. M. Raj, V. Ramamurthy and C. G. Elles, Spatial Confinement Alters the Ultrafast Photoisomerization Dynamics of Azobenzenes, *Chem. Sci.*, 2020, **11**(35), 9513–9523, DOI: 10.1039/d0sc03955a.

31 G. Gabor, Y. F. Frei and E. Fischer, Tautomerism and Geometric Isomerism in Arylazophenols and Naphthols. Spectra and Reversible Photoreactions of and p-Hydroxyazobenzene, *J. Phys. Chem.*, 1968, **193**(3), 3266–3272.

32 A. Cembran, F. Bernardi, M. Garavelli, L. Gagliardi and G. Orlandi, On the Mechanism of the *cis*-trans Isomerization in the Lowest Electronic States of Azobenzene: S0, S1, and T1, *J. Am. Chem. Soc.*, 2004, **8**, 3234–3243.

33 L. Schweighauser, M. A. Strauss, S. Bellotto and H. A. Wegner, Attraction or Repulsion? London Dispersion Forces Control Azobenzene Switches, *Angew. Chem., Int. Ed.*, 2015, **54**(45), 13436–13439, DOI: 10.1002/anie.201506126.

34 C. E. Weston, A. J. P. P. White, H. S. Rzepa, J. Contreras-garc, M. J. Fuchter, J. Calbo, C. E. Weston, A. J. P. P. White, H. S. Rzepa, J. Contreras-García and M. J. T. Fuchter, Azoheteroarene Photoswitch Performance through Heteroaryl Design, *J. Am. Chem. Soc.*, 2017, **139**(3), 1261–1274, DOI: 10.1021/jacs.6b11626.

35 S. Crespi, N. A. Simeth and B. König, Heteroaryl Azo Dyes as Molecular Photoswitches, *Nat. Rev. Chem.*, 2019, **3**(3), 133–146, DOI: 10.1038/s41570-019-0074-6.

36 Y. Ni, X. Li, J. Hu, S. Huang and H. Yu, Supramolecular Liquid-Crystalline Polymer Organogel: Fabrication, Multiresponsiveness, and Holographic Switching Properties, *Chem. Mater.*, 2019, **31**(9), 3388–3394, DOI: 10.1021/acs.chemmater.9b00551.

37 L. Cui and Y. Zhao, Azopyridine Side Chain Polymers: An Efficient Way to Prepare Photoactive Liquid Crystalline Materials through Self-Assembly, *Chem. Mater.*, 2004, **16**(11), 2076–2082, DOI: 10.1021/cm0348850.

38 H. Ren, X. Qiu, Y. Shi, P. Yang and M. Winnik, pH-Dependent Morphology and Photoresponse of Azopyridine-Terminated Poly(N-Isopropylacrylamide) Nanoparticles in Water, *Macromolecules*, 2019, **52**, 2939–2948, DOI: 10.1021/acs.macromol.9b00193.

39 T. Michinobu, R. Eto, H. Kumazawa, N. Fujii and K. Shigehara, Photochromism of Azopyridine Side Chain Polymer Controlled by Supramolecular Self-Assembly, *J. Macromol. Sci. Part Pure Appl. Chem.*, 2011, **48**(8), 625–631, DOI: 10.1080/15226514.2011.586279.

40 P. Dongare, A. G. Bonn, S. Maji and L. Hammarström, Analysis of Hydrogen-Bonding Effects on Excited-State Proton-Coupled Electron Transfer from a Series of Phenols to a Re(I) Polypyridyl Complex, *J. Phys. Chem. C*, 2017, **121**(23), 12569–12576, DOI: 10.1021/acs.jpcc.7b02449.

41 R. Fernández-Terá and L. Sévery, Living Long and Prosperous: Productive Intraligand Charge-Transfer States from a Rhenium(I) Terpyridine Photosensitizer with Enhanced Light Absorption, *Inorg. Chem.*, 2021, **3**(I), 1334–1343, DOI: 10.1021/acs.inorgchem.0c01939.

42 S. M. Martin, A. N. Oldacre, C. A. Pointer, T. Huang, G. M. Repa, L. A. Fredin and E. R. Young, Proton-Controlled Non-Exponential Photoluminescence in a Pyridylamidine-Substituted Re(I) Complex, *Dalton Trans.*, 2021, **50**(21), 7265–7276, DOI: 10.1039/d1dt01132d.

43 C. Schütt, G. Heitmann, T. Wendler, B. Krahwinkel and R. Herges, Design and Synthesis of Photodissociable Ligands Based on Azoimidazoles for Light-Driven Coordination-Induced Spin State Switching in Homogeneous Solution, *J. Org. Chem.*, 2016, **81**(3), 1206–1215, DOI: 10.1021/acs.joc.5b02817.

44 Z. J. Knepp, R. C. Hamburger, I.-A. Thongchai, K. Englehart, K. Sorto, A. Jaffer, E. R. Young and L. A. Fredin, Pinning Down Small Populations of Photoinduced Intermediates Using Transient Absorption Spectroscopy and Time-Dependent Density Functional Theory Difference Spectra to Provide Mechanistic Insight into Controlling Pyridine Azo Dynamics with Protons, *J. Phys. Chem. Lett.*, 2024, 9593–9600, DOI: 10.1021/acs.jpclett.4c02155.

45 D. A. Rodríguez-Soacha, S. A. M. Steinmüller, A. Işbilir, J. Fender, M. H. Deventer, Y. A. Ramírez, A. Tutov, C. Sotriffer, C. P. Stove, K. Lorenz, M. J. Lohse, J. N. Hislop and M. Decker, Development of an Indole-Amide-Based Photoswitchable Cannabinoid Receptor Subtype 1 (CB1R) "*cis*-On" Agonist, *ACS Chem. Neurosci.*, 2022, **13**(16), 2410–2435, DOI: 10.1021/acschemneuro.2c00160.

46 H. Gerwe, F. He, E. Pottie, C. Stove and M. Decker, Enlightening the "Spirit Molecule": Photomodulation of the 5-HT2A Receptor by a Light-Controllable N,N-Dimethyltryptamine Derivative, *Angew. Chem., Int. Ed.*, 2022, **61**(26), e202203034, DOI: 10.1002/anie.202203034.

47 N. A. Simeth, S. Crespi, M. Fagnoni and B. König, Tuning the Thermal Isomerization of Phenylazoindole Photoswitches from Days to Nanoseconds, *J. Am. Chem. Soc.*, 2018, **140**(8), 2940–2946, DOI: 10.1021/jacs.7b12871.

48 N. A. Simeth, A. Bellisario, S. Crespi, M. Fagnoni and B. König, Substituent Effects on 3-Arylazoindole Photoswitches, *J. Org. Chem.*, 2019, **84**(11), 6565–6575, DOI: 10.1021/acs.joc.8b02973.

49 S. Crespi, N. A. Simeth, A. Bellisario, M. Fagnoni and B. König, Unraveling the Thermal Isomerization Mechanisms of Heteroaryl Azoswitches: Phenylazoindoles as Case Study, *J. Phys. Chem. A*, 2019, **123**(9), 1814–1823, DOI: 10.1021/acs.jpca.8b11734.

50 M. J. Frisch, G. W. Trucks, H. B. Schlegel, G. E. Scuseria, M. A. Robb, J. R. Cheeseman, G. Scalmani, V. Barone, G. A. Petersson, H. Nakatsuji, X. Li, M. Caricato, A. V. Marenich, J. Bloino, B. G. Janesko, R. Gomperts, B. Mennucci, H. P. Hratchian, J. V. Ortiz, A. F. Izmaylov, J. L. Sonnenberg, D. Williams-Young, F. Ding, F. Lipparini, F. Egidi, J. Goings, B. Peng, A. Petrone, T. Henderson, D. Ranasinghe, V. G. Zakrzewski, J. Gao, N. Rega, G. Zheng, W. Liang, M. Hada, M. Ehara, K. Toyota, R. Fukuda, J. Hasegawa, M. Ishida, T. Nakajima, Y. Honda, O. Kitao, H. Nakai, T. Vreven, K. Throssell, J. A. Montgomery, J. E. Peralta, F. Ogliaro, M. J. Bearpark, J. J. Heyd, E. N. Brothers, K. N. Kudin, V. N. Staroverov, T. A. Keith, R. Kobayashi, J. Normand, K. Raghavachari, A. P. Rendell, J. C. Burant, S. S. Iyengar, J. Tomasi, M. Cossi, J. M. Millam, M. Klene, C. Adamo, R. Cammi, J. W. Ochterski, R. L. Martin, K. Morokuma, O. Farkas, J. B. Foresman and D. J. Fox, *Gaussian16 Revision C.01*, 2016.

51 T. Yanai, D. P. Tew and N. C. Handy, A New Hybrid Exchange-Correlation Functional Using the Coulomb-Attenuating Method (CAM-B3LYP), *Chem. Phys. Lett.*, 2004, **393**(1–3), 51–57, DOI: **10.1016/j.cplett.2004.06.011**.

52 R. Krishnan, J. S. Binkley, R. Seeger and J. A. Pople, Self-Consistent Molecular Orbital Methods. XX. A Basis Set for Correlated Wave Functions, *J. Chem. Phys.*, 1980, **72**(1), 650–654, DOI: **10.1063/1.438955**.

53 T. Clark, J. Chandrasekhar, G. Spitznagel and P. von Ragué Schleyer, Efficient Diffuse Function- Augmented Basis Sets for Anion Calculations. III.* The 3-21 + G Basis Set for First-Row Elements, Li-F, *J. Comput. Chem.*, 1983, **4**, 294–301, DOI: **10.1002/jcc.540040303**.

54 S. Grimme, S. Ehrlich and L. Goerigk, Effect of the Damping Function in Dispersion Corrected Density Functional Theory, *J. Comput. Chem.*, 2011, **32**(7), 1456–1465, DOI: **10.1002/jcc.21759**.

55 M. Cossi, V. Barone, R. Cammi and J. Tomasi, Ab Initio Study of Solvated Molecules: A New Implementation of the Polarizable Continuum Model, *Chem. Phys. Lett.*, 1996, **255**(4–6), 327–335, DOI: **10.1016/0009-2614(96)00349-1**.

56 A. H. Chen, Z. J. Knepp, C. A. Guzman, E. R. Young and L. A. Fredin, Intramolecular Subtleties in Indole Azo Dyes Revealed by Multidimensional Potential Energy Surfaces, *Phys. Chem. Chem. Phys.*, 2025, **27**, 6430–6437, DOI: **10.1039/D5CP00110B**.

57 R. C. Hamburger, T. Huang, S. M. Martin, C. A. Pointer, L. A. Fredin and E. R. Young, Ultra-Fast Excited-State Dynamics of Substituted trans-Naphthalene Azo Moieties, *Phys. Chem. Chem. Phys.*, 2023, **25**(22), 15302–15313, DOI: **10.1039/D3CP01211E**.

58 K. A. Connors, *Binding Constants: The Measurement of Molecular Complex Stability*, 1st edn, Wiley-Interscience, 1987.

59 A. Kütt, S. Tshepelevitsh, J. Saame, M. Lõkov, I. Kaljurand, S. Selberg and I. Leito, Strengths of Acids in Acetonitrile, *Eur. J. Org. Chem.*, 2021, (9), 1407–1419, DOI: **10.1002/ejoc.202001649**.

60 B. Maerz, S. Wiedbrauk, S. Oesterling, E. Samoylova, A. Nenov, P. Mayer, R. D. Vivie-riedle, W. Zinth and H. Dube, Making Fast Photoswitches Faster—Using Hammett Analysis to Understand the Limit of Donor–Acceptor Approaches for Faster Hemithioindigo Photoswitches, *Chem. – Eur. J.*, 2014, 13984–13992, DOI: **10.1002/chem.201403661**.

61 J. D. S. Ritter and S. I. Miller, The p-p Relation and the Reaction of trans-Cinnamic Acids with Diphenyldiazomethane The Basis of the Hammett Equation, *J. Am. Chem. Soc.*, 1964, **86**(8), 1507–1512, DOI: **10.1021/ja01062a012**.

62 S. L. Broman, M. Jevric and M. B. Nielsen, Linear Free-Energy Correlations for the Vinylheptafulvene Ring Closure: A Probe for Hammett σ Values, *Chem. – Eur. J.*, 2013, **19**(29), 9542–9548, DOI: **10.1002/chem.201300167**.

63 S. Böhm, P. Paŕík and O. Exner, Range of Validity of the Hammett Equation: Acidity of Substituted Ethynylbenzenes, *New J. Chem.*, 2006, **30**(3), 384, DOI: **10.1039/b512698c**.

64 M. S. Sigman and J. J. Miller, Examination of the Role of Taft-Type Steric Parameters in Asymmetric Catalysis, *J. Org. Chem.*, 2009, **74**(20), 7633–7643, DOI: **10.1021/jo901698t**.

65 W. Van Valkenburg, *Biological Correlations—The Hansch Approach,* American Chemical Society, 1974, DOI: **10.1021/ba-1972-0114**.

66 S. H. Unger and C. Hansch, Quantitative Models of Steric Effects, in *Progress in Physical Organic Chemistry*, ed. R. W. Taft, Wiley, 1976, vol. 12, pp 91–118, DOI: **10.1002/9780470171912.ch4**.

67 R. W. Taft, Linear Free Energy Relationships from Rates of Esterification and Hydrolysis of Aliphatic and Ortho-Substituted Benzoate Esters, *J. Am. Chem. Soc.*, 1952, **74**(11), 2729–2732, DOI: **10.1021/ja01131a010**.

68 J. O. Schreck, Nonlinear Hammett Relationships, *J. Chem. Educ.*, 1971, **48**(2), 103–107, DOI: **10.1021/ed048p103**.

69 M. I. Kabachnik, T. A. Mastrukova, A. E. Shipov and T. A. Melentyeva, The Application of the Hammett Equation to the Theory of Tautomeric Equilibrium, *Tetrahedron*, 1960, **9**(1–2), 10–28, DOI: **10.1016/0040-4020(60)80048-8**.

70 M. Charton, Steric Effects. 7. Additional V Constants, *J. Org. Chem.*, 1976, **41**(12), 2217–2220, DOI: **10.1021/jo00874a035**.

71 M. Charton, Steric Effects. I. Esterification and Acid-Catalyzed Hydrolysis of Esters, *J. Am. Chem. Soc.*, 1975, **97**(6), 1552–1556, DOI: **10.1021/ja00839a047**.

72 M. Charton, Steric Effects. II. Base-Catalyzed Ester Hydrolysis, *J. Am. Chem. Soc.*, 1975, **97**(13), 3691–3693, DOI: **10.1021/ja00846a022**.

73 H. Nishioka, X. Liang and H. Asanuma, Effect of the Ortho Modification of Azobenzene on the Photoregulatory Efficiency of DNA Hybridization and the Thermal Stability of Its Cis Form, *Chem. – Eur. J.*, 2010, **16**(7), 2054–2062, DOI: **10.1002/chem.200902789**.

74 J. García-Amorós and D. Velasco, Recent Advances towards Azobenzene-Based Light-Driven Real-Time Information-Transmitting Materials, *Beilstein J. Org. Chem.*, 2012, **8**, 1003–1017, DOI: **10.3762/bjoc.8.113**.

75 L. A. Fredin, M. Pápai, E. Rozsályi, G. Vankó, K. Wärnmark, V. Sundström and P. Persson, Exceptional Excited-State Lifetime of an Iron(II)– N -Heterocyclic Carbene Complex

Explained, *J. Phys. Chem. Lett.*, 2014, **5**(12), 2066–2071, DOI: **10.1021/jz500829w**.

76 L. A. Fredin and P. Persson, Influence of Triplet Surface Properties on Excited-State Deactivation of Expanded Cage Bis(Tridentate)Ruthenium(II) Complexes, *J. Phys. Chem. A*, 2019, **123**(25), 5293–5299, DOI: **10.1021/acs.jpca.9b02927**.

77 S. Devi, M. Saraswat, S. Grewal and S. Venkataramani, Evaluation of Substituent Effect in Z -Isomer Stability of Arylazo-1H-3,5-Dimethylpyrazoles: Interplay of Steric, Electronic Effects and Hydrogen Bonding, *J. Org. Chem.*, 2018, **83**(8), 4307–4322, DOI: **10.1021/acs.joc.7b02604**.

78 J. L. Magee, W. Shand and H. Eyring, Non-Adiabatic Reactions. Rotation about the Double Bond, *J. Am. Chem. Soc.*, 1941, **63**(3), 677–688, DOI: **10.1021/ja01848a012**.

79 S. M. Martin, R. C. Hamburger, T. Huang, L. A. Fredin and E. R. Young, Controlling Excited-State Dynamics via Protonation of Naphthalene-Based Azo Dyes, *Phys. Chem. Chem. Phys.*, 2024, **26**(14), 10804–10813, DOI: **10.1039/D4CP00242C**.